WAVELET-BASED BREAST TUMOR LOCALIZATION TECHNIQUE USING A UWB RADAR

A. Lazaro, D. Girbau, and R. Villarino

Department of Electronics, Electrics and Automatics Engineering
Universitat Rovira i Virgili (URV)
Av. Països Catalans 26, Campus Sescelades, 43007 Tarragona, Spain

Abstract—This paper deals with the potential of ultra-wideband (UWB) microwave imaging for the detection and localization of breast cancer in its early stages. A method is proposed for locating tumors which is based on the signal time-of-flight backscattered by the tumor. Time-of-flight is detected using a wavelet transform algorithm. The feasibility of the method has been investigated by means of simulated results using Finite-Difference Time-Domain (FDTD) and experimental results with a UWB radar and a phantom.

1. INTRODUCTION

The X-ray mammogram is the primary technique used in breast cancer detection today. However, this technique poses several problems, such as the use of ionizing radiation, breast compression, complications in its use on younger women [1], and difficulty in detecting early tumors. Microwave breast tumor detection is a non-invasive technique that uses non-ionizing radiation and it is considered a potential alternative to X-rays [1, 2]. The tumor detection principle is based on analyzing the contrast in the dielectric properties between the healthy and malignant tissues [1]. On the other hand, several techniques have recently been expanded — Concepts and circuits based on ultra-wideband (UWB) pulses especially for communication systems [3] — Which have also proved interesting for tomography applications. A number of imaging methods for ultra wideband microwave imaging of breast tumors are already available [1, 2, 4–9].

A UWB radar uses sub-nanosecond pulses to illuminate the space. If there is an object in the illumination area, a part of the transmitted pulse will be reflected and detected by the receiving

---

Corresponding author: A. Lazaro (antonioramon.lazaro@urv.cat).

antenna. Practical multilateration systems can be implemented using UWB technology [10]. In these systems, ranges are determined between the object and the known points by measuring the time-of-flight (or time-of-arrival, ToA) of a UWB signal between a transmitter and a receiver (placed at known positions). The measured time-of-flight can be converted into ranges by multiplying it by the (known) speed of light. In conventional correlation-based ToA estimation algorithms, the time shift of a template signal that produces the maximum correlation with the received signal is used to estimate the ToA [11]. In other words, correlations of the received signal with shifted versions of a template signal are considered. In a single path channel, the transmitted waveform can be used as the optimal template signal, and conventional correlation-based estimation can be employed. Therefore, the correlation of the received signal with the transmit-waveform template is suboptimal in a multipath channel. If this suboptimal technique is employed in a narrowband system, the correlation peak may not give the true ToA since multiple replicas of the transmitted signal partially overlap due to multipath propagation. Fortunately, due to the large bandwidth of a UWB signal, multipath components are usually resolvable without the use of complex algorithms. In fact, due to the very short pulse, the resolution of such radar is very high. Moreover, the sub-nanosecond pulse used possesses a very broad bandwidth which enables the penetration of the material.

In this work, a UWB radar using a wavelet transform algorithm is presented for breast tumor detection. When the transmitted pulse hits the breast surface, a pulse is backscattered towards the receiver, but a portion of the transmitted pulse propagates inside the breast and is reflected by reflecting objects such as a region of tumor tissue. Due to the high resolution of UWB radars, the reflected pulses can be separated. The matched filter concept can detect the position as well as the intensity of a specific pulse covered by noise but, to do that, knowledge of the exact shape of the pulse is required. Unfortunately this information is not available in real UWB systems since, as stated, there are several potential sources of pulse distortion during propagation: Distortion as it passes through a material or distortion due to diffraction. Therefore, the received pulse, as a first approximation, is a scaled and time-shifted version of the transmitted pulse. In order to overcome this drawback, this work proposes using the Continuous Wavelet Transform (CWT) as a multiscale matched filter [12–15].

The Continuous Wavelet Transform (CWT) can handle different stretched pulses, but the basic shape of the sought impulse still has to

be known a priori. However, by using a complex extension to the signal, as well as to the wavelet, as presented in [14], this drawback can be eliminated. In essence, the CWT performs a correlation analysis [12] and as a consequence, maximum output can be expected when the input signal most resembles the wavelet template, $W(a, \tau)$ (a is the scale and τ is the delay). This principle is the basis of the matched filter, which is the optimum detector of a deterministic signal in the presence of additive noise. Consider the measurement model where the received signal $s(t)$ is composed of the scaled transmitted pulse with noise, $s(t) = p_a(t - \tau) + n(t)$ where $p_a(t) = p(t/a)$ is a known deterministic pulse at scale a, τ an unknown location parameter, and $n(t)$ an additive white Gaussian noise component. Classical detection theory tells us that the optimal procedure for estimating τ is to perform the correlation with all the possible shifts in our reference template (convolution) and to select the position that corresponds to the maximum output (maximum likelihood solution). So, it makes sense to use a CWT-like detector whenever the pattern $p(t)$ which we are looking for can appear at various scales. Therefore, the CWT can be used to determine the ToA of reflected pulses [13–15].

After identifying the reflections on the tumor at several antenna positions, its position can be located [16]. However, in contrast with [16], where only numerical results were presented and it was assumed that the breast-skin interface was perfectly matched, this work considers air-coupled antennas (a more realistic case) and experimentally validates that technique.

This paper is organized as follows. Section 2 describes the experimental setup developed to validate the proposed techniques using a phantom. Section 3 describes the measurement of ToA using the Continuous Wavelet Transform. The localization algorithm and background subtraction technique are presented in Section 4. In Section 5, the performance of the calibration technique and location algorithms are investigated using synthetic measures obtained from Finite-Difference Time-Domain (FDTD) simulations. A sensibility study of the variations in the breast relative dielectric permittivity is also presented. In Section 6, the experimental results using a UWB radar and a phantom are described. Finally, conclusions are drawn in Section 7.

2. UWB SYSTEM

A UWB radar test setup was built to obtain experimental results using a phantom (see Fig. 1). The GZ1120ME-50EV pulse generator from Geozondas is used to generate a monocycle pulse of 5 GHz
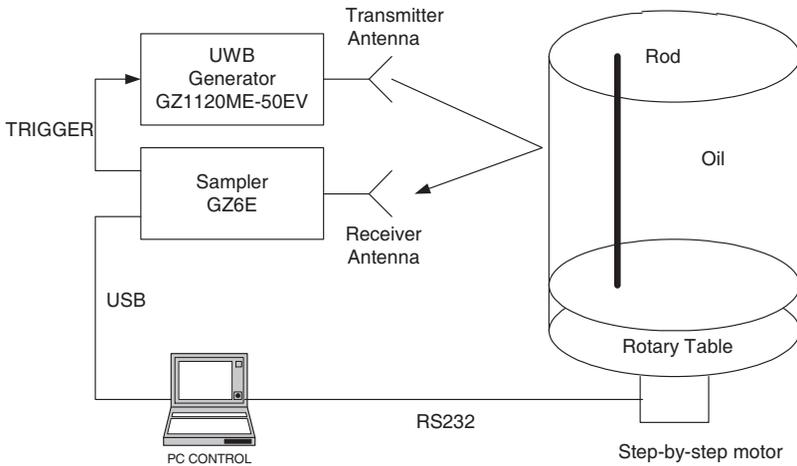
Figure 1. UWB-radar test setup.

central frequency, amplitude of $\pm 5\,\text{V}$ and a pulse repetition rate (PRI) of 250 kHz. The output of the pulse generator is connected to a UWB transmitter antenna (3.1–10.6 GHz frequency range). In this experiment a phantom has been designed to simulate the scene (see Fig. 1). A low-permittivity rod is used to simulate the tumor. The rod is immersed in an oil-filled cylindrical glass tank. The skin is simulated using the cylindrical surface of the tank and the antennas are air coupled [9]. Thus, considerable reflections are expected in the skin. A high mismatch between air and skin simplifies the detection of the breast contour. Since the antenna pattern is not directive, several reflections from surrounding objects are collected. To create a synthetic array, antennas are at a fixed position, the phantom is physically rotated and measurements are repeated at each location.

The radiated pulse is reflected in the phantom and detected using a receiver antenna. Sampling is done with the GZ6E sampler converter from Geozondas, which triggers the pulse generator. As known from the Cramer-Rao lower bound for single-path channels, the deviation in the determination of ToA is inversely proportional to the system bandwidth and the square of the signal-to-noise ratio [10]. Thus, there is a compromise; decreasing the pulse duration improves resolution but, since losses of the breast increase with the frequency, the signal-to-noise is degraded, and precision in the determination of ToA may be reduced.

3. COMPLEX CONTINUOUS WAVELET TRANSFORM (CWT) FOR DELAY ESTIMATOR

The CWT of a complex signal $s(t)$ is defined as the cross-correlation between the signal and the scaled, stretched and shifted mother wavelet ψ_n (convolution). At time τ and scale a this transformation is defined as [12]:

$$W_s(a, \tau) = s(\tau) * \left(\frac{1}{\sqrt{a}} \psi_n^* \left(\frac{\tau}{a} \right) \right) = \int_{-\infty}^{+\infty} s(t) \frac{1}{\sqrt{a}} \psi_n^* \left(\frac{t - \tau}{a} \right) dt \quad (1)$$

The weights $W_s(a, \tau)$ are complexes. Several wavelet families have been proposed in the literature as a function of the application [12]. In this case, complex Gaussian wavelets have been selected since typical UWB radars generate Gaussian-like shaped pulses or their derivatives. The n-th order complex Gaussian wavelet is obtained from the n-th derivative of the complex Gaussian function:

$$\psi_n(t) = C_n \frac{d^n}{dt^n} \left(e^{-jt} e^{-t^2} \right) \quad (2)$$

where C_n is a normalization constant such that the 2-norm of $\psi_n(t)$ is. If n is even, the real part of ψ_n is an even function and the imaginary part is odd, and vice versa for an odd n. Therefore, the real and imaginary parts of the wavelet are orthogonal.

Instead of using the received signal $s(t)$, the analytical signal $s^+(t)$ can be used [14], whose real part is $s(t)$ and the imaginary part is obtained from its Hilbert transform:

$$s^+(t) = s(t) + jH\{s(t)\} \quad (3)$$

It is known that the signal $s(t)$ and its Hilbert transform are orthogonal (4) and for the special case of even functions the Hilbert transform is odd and vice versa.

$$\int_{-\infty}^{+\infty} s(t)H\{s(t)\} dt = 0 \quad (4)$$

As discussed in the introduction, the CWT coefficients can be interpreted as the output of a matched filter or correlator. If the input signal $s(t)$ is a scaled and shifted version of ψ_n, the coefficient is maximum when:

$$s(t) = k\psi_n \left(\frac{t - \tau}{a} \right) \quad (5)$$
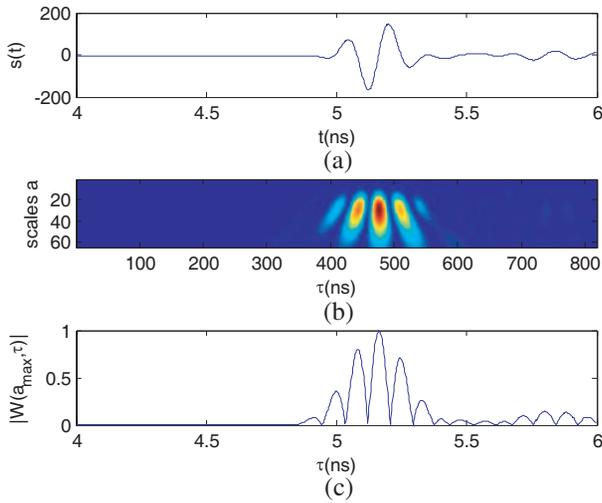
Figure 2. (a) Measured time signal $s(t)$, (b) magnitude of the CWT of $s(t)$ using 3rd order complex Gaussian wavelet, and (c) cut of the CWT for the scale of the peak magnitude.
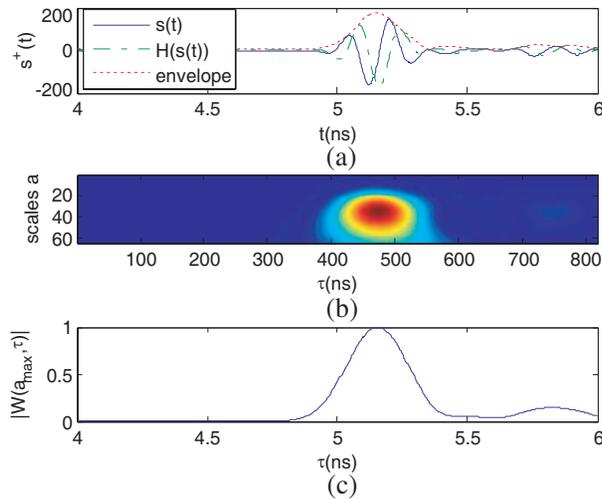
Figure 3. (a) Measured time signal $s(t)$, its Hilbert transform $H(s(t))$ and the envelope of the analytical signal $s^+(t)$, (b) magnitude of the CWT of $s^+(t)$ using 3rd order complex Gaussian wavelet, and (c) cut of CWT for the scale of the peak magnitude.

where k is a scale constant. So, the arguments of the CWT, a_m and τ_m, specify the dilatation and translation or delay, which characterize the received pulse.

$$(a_m, \tau_m) = \arg\max(a, \tau) \{|W(a, \tau)|\} \qquad (6)$$

where τ_m is the delay (or time-of-flight or ToA) of the received pulse.

The UWB generator used in the experimental setup generates a Gaussian monocycle pulse. Fig. 2(a) shows the pulse measured at the sampler. The differentiation effect of the antennas can be observed. The CWT of $s(t)$ is calculated using a 3rd order complex Gaussian wavelet ($n = 3$). Due to the ability of CWT to adjust non-symmetrical pulses, similar results could be obtained if other orders were used. The magnitude of the CWT is shown in Fig. 2(b). A cut of the wavelet transform for the peak scale value is shown in Fig. 2(c). The maximum of the wavelet transform indicates the time delay of the pulse. However, some side maxima separate from the main peak appear [14]. In the case of heavy noise this drawback may make separating targets impossible due to multiple reflections. Fig. 3(a) shows the measured signal $s(t)$ (real part of the analytical signal $s^+(t)$), its Hilbert transform (imaginary part of $s^+(t)$) and the envelope of $s^+(t)$. The detection
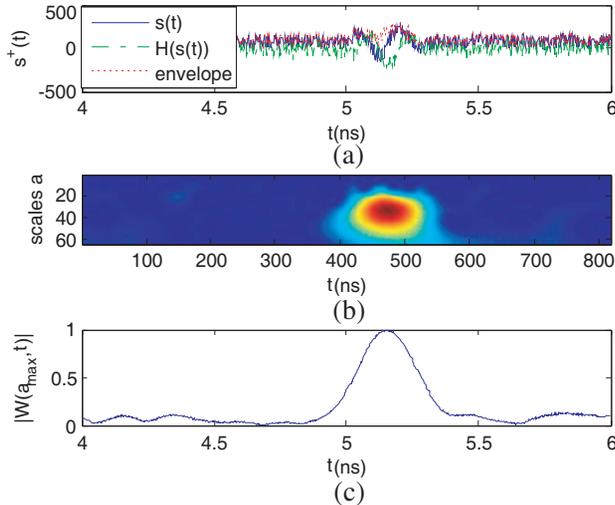
Figure 4. (a) Measured time signal $s(t)$ with added noise (SNR = 0 dB), its Hilbert transform $H(s(t))$ and the envelope of the analytical signal $s^+(t)$, (b) magnitude of the CWT of $s^+(t)$ using 3rd order complex Gaussian wavelet, and (c) cut of CWT for the scale of the peak magnitude.
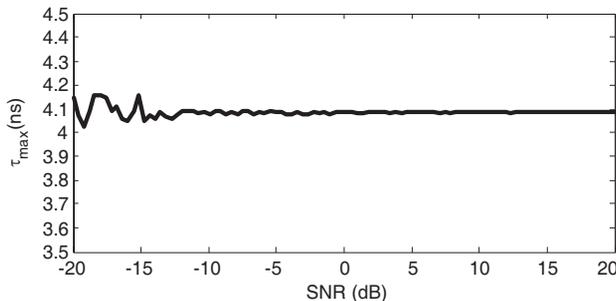
Figure 5. ToA detected from the peak of the magnitude of CWT as a function of the signal-to-noise ratio (SNR) in dB.

of the envelope peak can be used to determine the ToA of the signal; however, in the presence of noise, it may be difficult to determine this peak. The magnitude of CWT of the complex analytical signal $s^+(t)$ is shown in Fig. 3(b). Now, the CWT presents only one maximum [14] that can be easily detected even in the presence of noise. In order to investigate the effect of noise, uniform-distributed noise is added to the signal to simulate the quantification noise in the sampler. In Fig. 4, the same analysis as in Fig. 3 is repeated but adding noise with a signal-to-noise ratio (SNR) of 0 dB. The SNR is defined as the square of the peak amplitude of the pulse to noise variance. Due to the presence of noise, the maximum of the envelope is difficult to detect, but it can be easily detected from the CWT of the analytical signal $s^+(t)$. Fig. 5 shows the ToA (τ_{max}) detected from the CWT of the analytical signal as a function of the SNR. This result shows the robustness of the CWT as a matched filter or correlator, but with the advantage that the template signal of the generator does not have to be known beforehand.

4. LOCALIZATION TECHNIQUE

4.1. Localization Algorithm

Figure 6 shows a typical situation. The transmitted pulse propagates by air (or coupling medium) to the breast. By means of the coupling between the transmitter and receiver antennas, a pulse is directly coupled to the receiver. This pulse can be easily eliminated using an appropriate time-gating window. The next received pulse is due to skin reflection. Part of the energy penetrates the breast and can be reflected on a tumor because the dielectric properties of tumors differ from those of healthy tissues. Multiple reflections on the skin interface and other
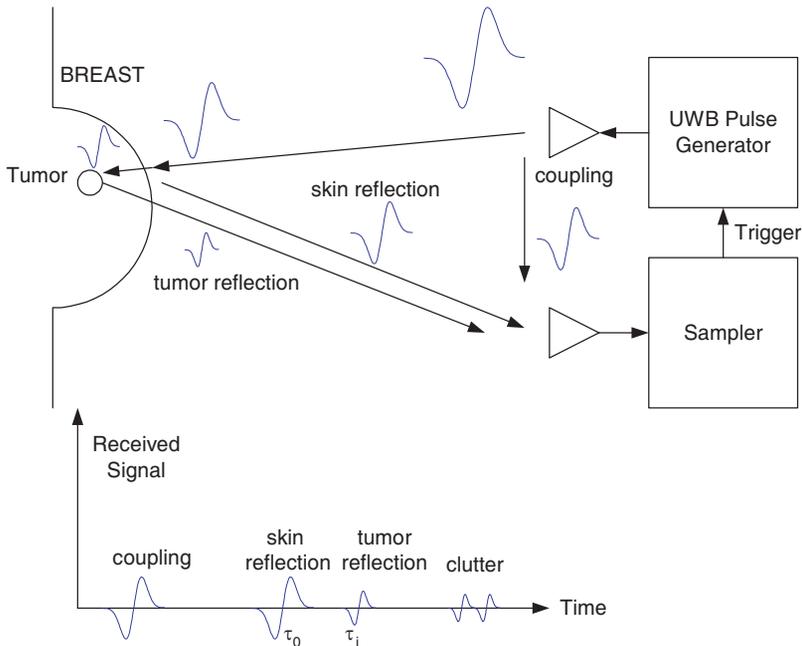
Figure 6. Multiple reflections diagram in a breast.

objects are expected to arrive later than tumor reflections and can be considered as clutter. Since the setup has cylindrical symmetry and the two antennas are close to one another, a monostatic situation can be considered for calculations. So, the time-of-flight associated with tumor pulse reflection can be expressed as:

$$\tau_i = \frac{2}{c/\sqrt{\varepsilon_r}}\sqrt{(x-x_i)^2 + (y-y_i)^2 + (z-z_i)^2} + \tau_{0i} + \tau_0 \qquad (7)$$

where c is the vacuum light velocity, ε_r is the relative dielectric permittivity of the breast, τ_{0i} is the propagation time between the antenna and the skin surface, (x_i, y_i, z_i) is the antenna position and (x, y, z) is the unknown tumor position. The delay τ_0 is a systematic delay between transmitter and receiver due to antenna cables and other system delays (such as those introduced by antennas and receiver synchronization). Although this delay could be obtained by means of a calibration of the reflected pulse by using a metallic plate at a known distance, it can also be considered as another unknown.

The propagation time τ_{0i} can be obtained using the CWT as explained in the previous Section from the measured signal for each antenna position i, $s_i(t)$. Next, a skin retrieval algorithm is applied

to separate the tumor reflections. The application of the skin retrieval algorithm is important, since reflections on the tumor have much lower amplitude than reflections on the skin; however, these reflections are almost independent of the antenna measurement point. Using an appropriate time window, reflections from distant objects and other multiple reflections considered as part of the clutter are eliminated, resulting in a corrected signal $r_i(t)$. After this clutter reduction, the time-of-flight due to tumor reflection (7) is obtained from the CWT of $r_i(t)$. The procedure is repeated for each antenna position in order to obtain a system of Equation (7) with more equations than unknowns. A block diagram of this algorithm is shown in Fig. 7. Note that, in contrast with confocal microwave breast detection methods [1, 2, 4–9], the contour surface of the breast does not have to be known or determined [17], which is a great advantage in clinical cases.

To compute the unknown position of the tumor in the ToA system of equations, a non-linear model is fitted to multiple pseudoranges and the positions of the known antenna points. The pseudoranges are obtained from (7):

$$\rho_i = \sqrt{(x - x_i)^2 + (y - y_i)^2 + (z - z_i)^2} = \frac{1}{2}c/\sqrt{\varepsilon_r}(\tau_i - \tau_{0i} - \tau_0) \quad (8)$$

Here τ_i and τ_{0i} are the estimated ToA at the i-th antenna and $c/(\varepsilon_r)^{1/2}$ is the speed of light in the breast. From (8), the following non-linear system of equations (equal to the number of antenna positions, N) can be obtained.

$$f_i(x, y, z, \tau_0) = \sqrt{(x - x_i)^2 + (y - y_i)^2 + (z - z_i)^2}$$
$$-2c/\sqrt{\varepsilon_r} \cdot (\tau_i - \tau_{0i} - \tau_0) = 0, \quad i = 1, \ldots, N \quad (9)$$
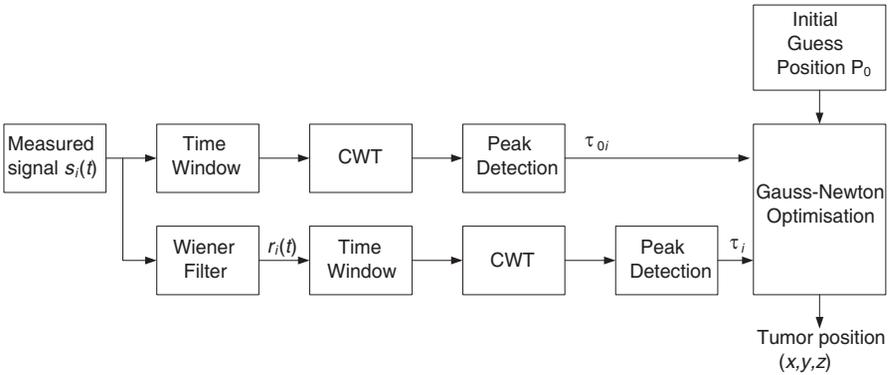
Figure 7. Block diagram of the localization algorithm.

In Equations (7)–(9), the average permittivity value over the UWB frequency band is used.

An objective function is normally required for any optimization algorithm. Since the ultimate aim of positioning is to obtain an accurate position estimation, it is natural to define the objective function as the sum of the squared range errors of all antenna positions:

$$F(x, y, z, \tau_0) = \frac{1}{2} \sum_{i=1}^{N} f_i^2 \qquad (10)$$

The purpose of optimization is to minimize this objective function to produce the optimal position estimation. For notational simplicity, we define:

$$p = (x, y, z, \tau_0)^T \qquad (11)$$
$$f(p) = (f_1, f_2, \ldots, f_N)^T \qquad (12)$$

The Gauss-Newton algorithm is a method used to solve non-linear least squares problems. It can be seen as a modification of Newton's method for finding a minimum of a function. Unlike Newton's method, the Gauss-Newton algorithm can only be used to minimize a sum of squared function values, but it has the advantage that second derivatives, which can be challenging to compute, are not required. Starting with an initial guess p_0 for the minimum, the method proceeds by the iterations:

$$p_{k+1} = p_k + \mathbf{\Delta} \qquad (13)$$

The Gauss-Newton algorithm can be derived by linearly approximating the vector of functions f_i. Using Taylor's theorem, at every iteration it can be written as:

$$f(p_{k+1}) \approx f(p_k) + \mathbf{J}_k \cdot \mathbf{\Delta} \qquad (14)$$

where $\mathbf{J}_k$ is the Jacobian matrix evaluated at iteration k. Assuming that $f(p_{k+1})$ is zero, the increment $\mathbf{\Delta}$ is the solution to the normal equations:

$$\mathbf{J}_k^T \mathbf{J}_k \Delta = -\mathbf{J}_k^T f(p_k) \qquad (15)$$

The assumption that $N > 3$ in the algorithm statement is necessary, as otherwise the matrix $\mathbf{J}_k^T \mathbf{J}_k$ can not be inverted and the normal equations can not be solved. The normal equations are N linear simultaneous equations in the unknown increments, $\mathbf{\Delta}$. The Jacobian matrix can be analytically obtained from the differentiation of (8):

$$\mathbf{J}_k = \left[\begin{array}{cccc} \frac{x_k - x_i}{|\rho_{i,k}|} & \frac{y_k - y_i}{|\rho_{i,k}|} & \frac{z_k - z_i}{|\rho_{i,k}|} & -\frac{1}{2}c/\sqrt{\varepsilon_r} \end{array} \right]_{i=1\cdots N} \qquad (16)$$

with

$$|\rho_{i,k}| = \sqrt{(x_k - x_i)^2 + (y_k - y_i)^2 + (z_k - z_i)^2} \qquad (17)$$

4.2. Background Subtraction

As stated earlier, the reflected pulse at the skin-air interface is greater than the reflection at the tumor tissue. Pulses reflected at the skin can be partially eliminated using calibration. Calibration can be done by measuring the time response without the sample (clutter or background) and subtracting it from the measured signal (now with the rod) at each angular position. This technique is known as background subtraction. However, this technique does not correct the effect of skin reflections in a real breast. A more appropriated method consists of subtracting the average value at each angular position since, if the contributions to the signal that are common to all angular positions do not depend on the tumor (or rod, in the case of the phantom), these would compensate themselves. In this case, instead of subtracting the average value of the signals, the weighted average is subtracted. This can be implemented by means of a Wiener filter [9].

Finally, the signal $r_i(t)$ at the output of the Wiener filter is time windowed to eliminate clutter from distant objects. Then, by applying the CWT to the windowed $r_i(t)$ and using (7), the time delay τ_i between transmitter and receiver due to the backscattering at the tumor is obtained. The procedure is repeated for each antenna position in order to obtain an over-determined system (9). After that, the tumor position is calculated using the Gauss-Newton optimization method (15).

5. SIMULATED RESULTS

The scattering observed in high-contrast objects was analyzed using the Finite-Difference Time-Domain (FDTD) method [19]. The response of 32 antennas uniformly distributed around a simulated breast was obtained. A 5-GHz *ricker*-pulse (Gaussian derived pulse) was injected. The antennas were uniformly distributed in a 6-cm radius around the breast and were not immersed in any gel. The simulation used a 5-cm radius cylindrical surface. Permittivity values of skin and of healthy and malignant tissues were obtained from [20] (see Table 1). The permittivity expression (18), known as the Debye model, was used; it includes a frequency-dispersion model and takes into account typical conductivities. The simulated tumor was emulated by 0.25, 0.5 and 1-cm diameter rods.

$$\varepsilon_{rc} = \varepsilon_r(\infty) + \frac{\varepsilon_r(0) - \varepsilon_r(\infty)}{1 + j\omega\tau} + \frac{\sigma}{j\omega\varepsilon_0} \tag{18}$$

where $\varepsilon_r(0)$ and $\varepsilon_r(\infty)$ are the DC and high-frequency relative permittivities, respectively, σ the conductivity and τ the constant that controls frequency dispersion.

Table 1. Permittivity parameters used in the model (18).

Tissue	ε_r (∞)	ε_r (0)	σ (S/m)	τ (ps)
Skin	4	37	1.1	7.23
Breast type 1	7	10	0.15	7
Breast type 2	6.57	16.29	0.23	7
Malignant	3.99	54	0.7	7
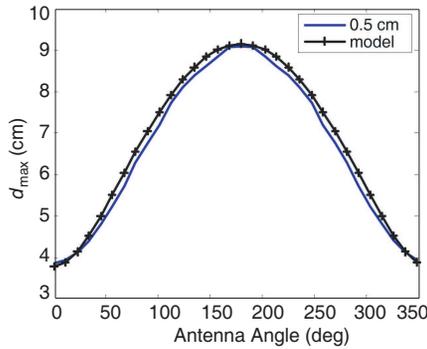
Figure 8. Distance between the antenna and the maximum reflectivity point as a function of the angle of antenna used in reception.

Several cases were simulated. Fig. 8 shows the distance from the antenna to the maximum reflectivity point (associated to the tumor obtained from the CWT of simulated data with breast type 1 and a 0.5-cm diameter tumor), as a function of the angle. The simulations were compared with the distance calculated from the theoretical model considering a perfect reflectivity point and good agreement was obtained. The position of the tumor can be derived from this figure. The distance to the center was obtained as the midpoint between the maximum distance and minimum distance, and the angular position of the tumor can be obtained from the angle where the distance between the antenna position and the tumor is minimum. In this case, the exact position is $(x, y, z) = (2.68, 0, 0)$ cm, thus the minimum distance is for the 0 degree antenna position. The tumor position can be graphically obtained by intercepting the circles with the center at each antenna position and radius equal to the distance to the tumor, as shown in Fig. 9, where the position computed using the optimization procedure (13)–(17) for different positions and tumor diameters is also plotted. This figure also shows that the diameter of the tumor can also be estimated.
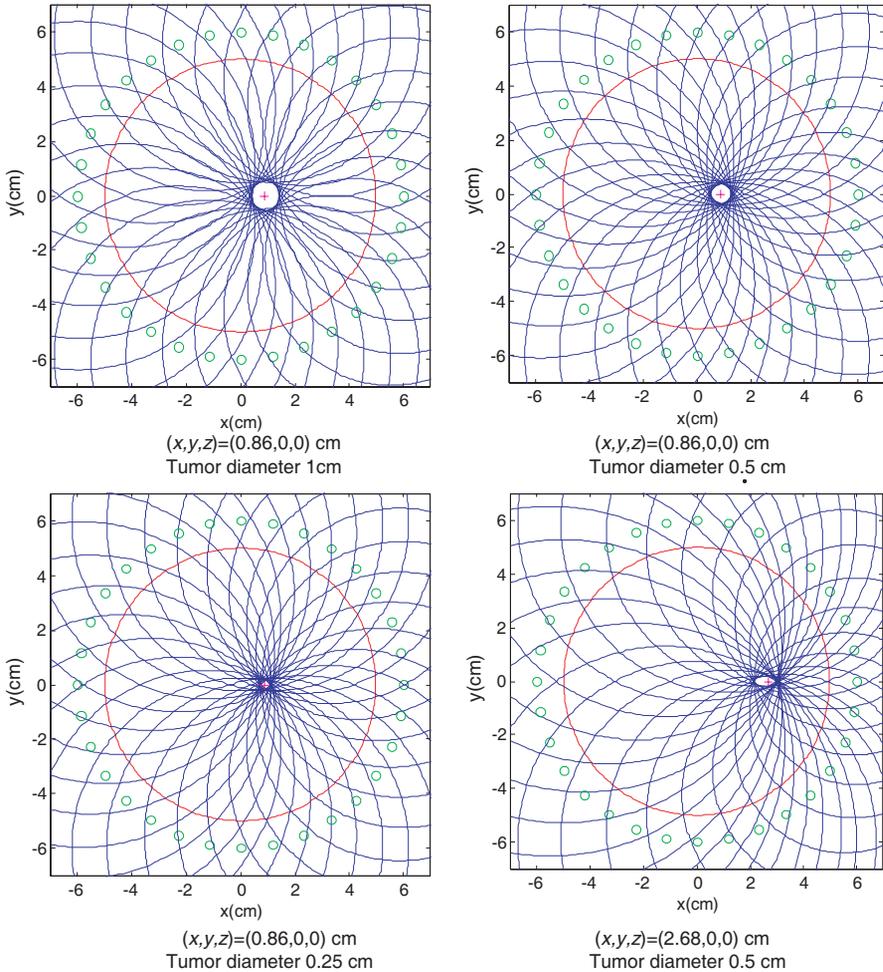
Figure 9. Graphic determination of the tumor position obtained by interception of the circles with center at each antenna position for different positions and tumor diameters. Tumor positions computed using the optimization procedure (13)–(17) are indicated with the cross points (+).

Just as with the calculation of the pseudoranges in (8), the velocity of propagation in the breast must also be known. This velocity is a function of permittivity, which can vary from person to person and is a function of the frequency. Sensitivity to changes in breast permittivity has been studied. The change in skin permittivity can be neglected,
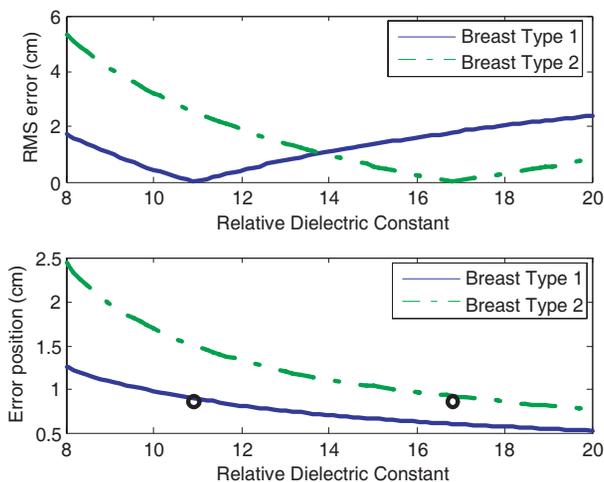
Figure 10. Mean RMS error and position found by the optimization algorithm as a function of the relative dielectric constant from breast type 1 and type 2. The exact tumor position is marked with a circle (o).

since the delay introduced in the skin is small compared to the propagation time within the breast. Tumor permittivity only affects the amplitude of the reflected pulse; by using the proposed method its value has not to be known. From the optimization algorithm, the mean RMS error can be computed using:

$$\sigma = \sqrt{\frac{1}{N} \sum_{i=1}^{N} f_i^2} \tag{19}$$

Figure 10 shows the mean RMS error as a function of relative permittivity of the breast. The RMS error presents a clear minimum for the mean relative permittivity of the breast. This value shows that the error in the determination of the real position is very small (smaller than tumor radius). This feature could be used to find real breast permittivity in real measurements.

6. EXPERIMENTAL RESULTS

A 0.5-cm diameter rod was immersed in a cylinder with a 6 cm radius filled with vegetal oil (nominal dielectric permittivity of 2.5). The measurement setup is described in Fig. 1. Fig. 11 shows the measured
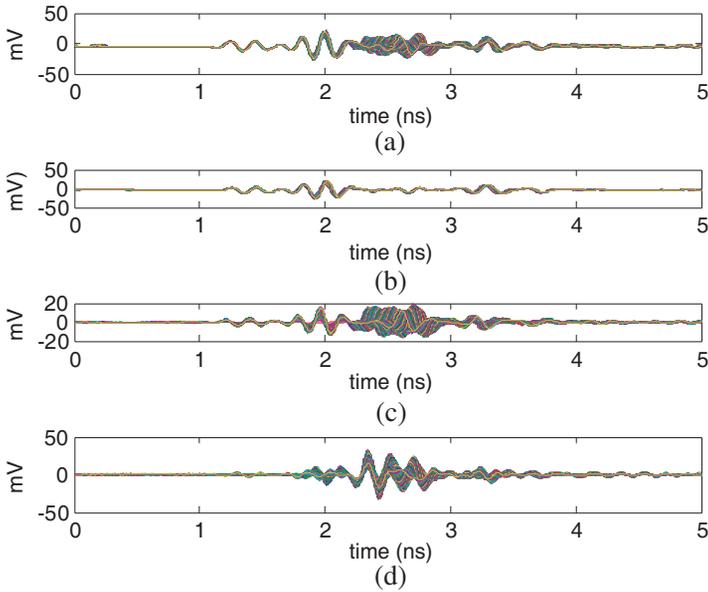
Figure 11. (a) Measured signal with the rod, (b) measured background signal without the rod, (c) signal after background subtraction, and (d) signal after the skin retrieval algorithm based on Wiener filter.
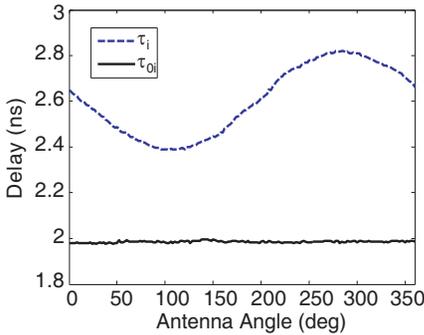
Figure 12. Measured time-of-flight between antenna and cylinder surface, τ_{0i}, and between the antenna and rod, τ_i, as a function of the antenna angle.
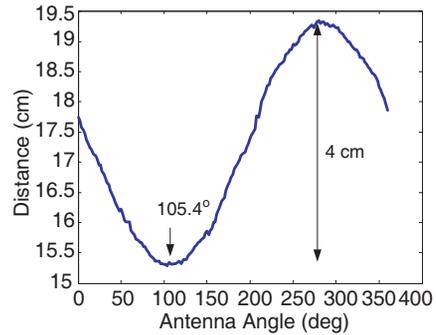
Figure 13. Measured distance between the antenna and the rod as a function of the antenna angle, calculated from the peak detection of the CWT.

time signal with the rod (Fig. 11(a)) and the background signal without the rod (Fig. 11(b)) for each antenna position. Comparing these figures, the signal around 1.4–1.5 ns corresponds to the coupling between the transmitter and receiver, whereas the signal around 2 ns corresponds to backscattering on the cylinder surface. The interesting part of the signal associated to the rod response is between 2.3 and 2.8 ns. Fig. 11(c) shows the signal after subtraction of the background and Fig. 11(d) the calibrated signal after the skin retrieval algorithm based on the Wiener filter. These figures show the suitability of the Wiener filter in eliminating clutter signal contribution from the cylinder surface and antenna coupling.

Figuer 12 plots the measured time-of-flight associated with the cylinder surface τ_{0i} (obtained from the peak detection of the CWT of Fig. 11(a)) and the measured time-of-flight associated with the pulse reflected at the rod (or tumor) τ_i (obtained from the peak detection of the CWT of Fig. 11(d)) for each antenna position. It is clear in this case that τ_{0i} is constant at 1.99 ns. However, it would be different for each antenna position if the skin surface of the phantom was not uniform.

The next step is the calculation of the pseudoranges from the time-of-flight τ_{0i} and τ_i using (8). For these calculations, the nominal dielectric permittivity of the oil is assumed ($= 2.5$). Fig. 13 shows the distance between the reflected pulse due to the rod and the antenna position as a function of the antenna angle. The rod is located 2 cm
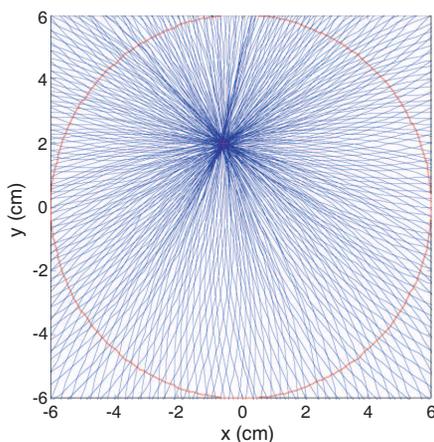
Figure 14. Interception of the circles for the tumor located at $(-0.054, 1.96)$ cm or $(2\,\text{cm} < 105.4°)$ in polar coordinates. The cross point (+) indicates the position obtained by optimization.
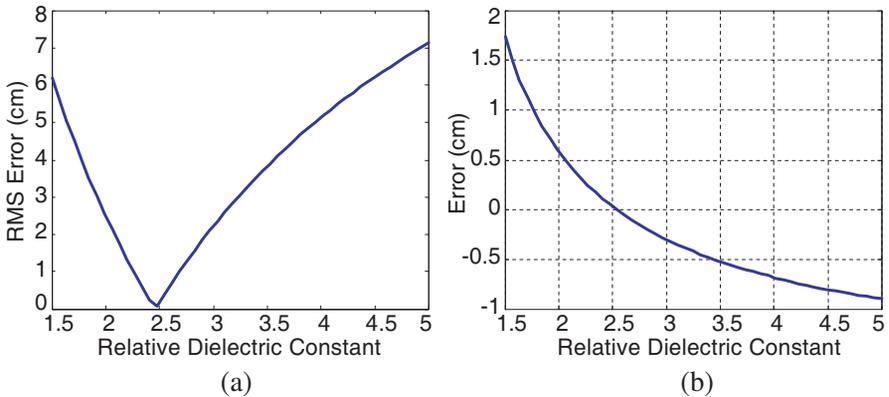
Figure 15. Mean RMS error (a) and error in the position (b) as a function of the relative dielectric constant for the measured scene.

from the cylinder center and at an angular position of 105.4°. The interception of the circles and the position of the rod located using the optimization confirm this position (see Fig. 14). As explained before, permittivity could be an unknown value in real clinical cases due to variability among persons. Fig. 15 shows the mean RMS error and the error position between the measured position and the real position as a function of the dielectric permittivity of the liquid. The minimum RMS error and zero error position is for the real value of the permittivity of the oil ($= 2.5$).

7. CONCLUSION

In this paper, a feasibility study of microwave imaging for breast tumor detection using UWB has been presented. In contrast to microwave breast imaging based on focusing techniques, the technique proposed in this paper is based on the localization of the tumor position using the time-of-flight of backscattered UWB pulses. A key point is the detection of the time-of-flight of reflected pulses. The optimal detector is based on the matched filter; however, as pulses are distorted in propagation through dispersive mediums, diffraction and multipath propagation, it is difficult to know it beforehand. To overcome this problem a detection technique based on the Continuous Wavelet Transform (CWT) has been proposed. The robustness of this technique in the presence of noise has been proven and a procedure for determining the pseudorange from the time-of-flight based on three steps has been introduced. In a first step, the time-of-flight

to the skin surface is obtained from the peak of the CWT signal. Next, a Wiener-filter skin-breast artifact removal algorithm is used to eliminate the clutter associated with the skin and the response of the antennas. Finally, the time-of-flight associated with the tumor reflection is obtained from the peak of the calibrated CWT signal. In the technique proposed here, the skin surface contour does not have to be known and only the mean relative permittivity of the breast has to be known a priori. This is a great advantage compared to other imaging techniques where the skin contour and dielectric permittivity and losses of the breast must be known beforehand. The position of the tumor is obtained graphically from the intersection of the circles with the center in the antenna position and a radius equal to the range to tumor for each antenna position. In addition, an optimization algorithm based on the Gauss-Newton method is also proposed in order to obtain the tumor position. It has been shown from FDTD numerical synthetic data and real measurements with a phantom that the mean RMS error is minimized for the real value of breast dielectric constant. This result could be used to obtain the permittivity value of the measurement by sweeping the RMS error obtained from the optimization algorithm as a function of breast permittivity. Experimental results using a phantom and a UWB radar have shown the feasibility of the proposed technique. These results open the door to low-cost micropower impulse transceivers for the early detection of breast cancer.

ACKNOWLEDGMENT

REFERENCES

1. Fear, E. C., J. Sill, and M. A. Stuchly, "Experimental feasibility study of confocal microwave imaging for breast tumor detection," *IEEE Trans. Microwave Theory Tech.*, Vol. 51, No. 3, 887–892, 2003.

2. Sill, J. M. and E. C. Fear, "Tissue sensing adaptive radar for breast cancer detection — Experimental investigation of simple tumor models," *IEEE Trans. Microwave Theory Tech.*, Vol. 53, No. 11, 3312–3319, 2005.

3. Fontana, R. J., "Recent system applications of short-pulse ultra-wideband (UWB) technology," *IEEE Trans. Microwave Theory Tech.*, Vol. 52, No. 9, 2087–2104, September 2004.

4. Klemm, M., I. Craddock, J. Leendertz, A. Preece, and R. Benjamin, "Experimental and clinical results of breast cancer detection using UWB microwave radar," *IEEE Antennas and Propagation Society International Symposium, AP-S 2008*, 1–4, 2008.

5. Craddock, I. J., M. Klemm, J. Leendertz, A. W. Preece, and R. Benjamin, "An improved hemispeherical antenna array design for breast imaging," *Proceedings European Conference on Antennas and Propagation, EuCAP 2007*, 1–5, 2007.

6. Meaney, P. M., M. W. Fanning, L. P. Dun, S. P. Poplack, and K. D. Paulsen, "A clinical prototype for active microwave imaging of the breast," *IEEE Trans. Microwave Theory Tech.*, Vol. 48, No. 11, 1841–1853, 2000.

7. Bindu, G., A. Lonappan, V. Thomas, C. K. Aanandan, and K. T. Mathew, "Active microwave imaging for breast cancer detection," *Progress In Electromagnetics Research*, PIER 58, 149–169, 2006.

8. Zhang, H., S. Y. Tan, and H. S. Tan, "A novel method for microwave breast cancer detection," *Progress In Electromagnetics Research*, PIER 83, 413–434, 2008.

9. Lazaro, A., D. Girbau, and R. Villarino, "Simulated and experimental investigation of microwave imaging using UWB," *Progress In Electromagnetics Research*, PIER 94, 263–280, 2009.

10. Sahinoglu, Z., S. Gezici, and I. Guvenc, *Ultra-wideband Positioning Systems*, Cambridge University Press, 2008.

11. Knapp, C. and G. Carter, "The generalized correlation method for estimation of time delay," *IEEE Trans. Acoust., Speech, and Sig. Processing (ICASSP)*, Vol. 24, 320–327, 1976.

12. Goswami, J. C. and A. K. Chan, *Fundamentals of Wavelets, Theory, Algorithms, and Applications*, John Wiley & Sons, Inc., 1999.

13. Li, H. J. and K. M. Li, "Application of wavelet transform in target identification," *Progress In Electromagnetics Research*, PIER 12, 57–73, 1996.

14. Pourvoyeur, K., A. Stelzer, G. Ossberge, T. Buchegger, and M. Pichle, "Wavelet-based impulse reconstruction in UWB-Radar," *IEEE MTT-S Digest*, 603–606, 2003.

15. Aly, O. A. M., A. S. Omar, and A. Z. Elsherbeni, "Detection and localization of RF radar pulses in noise environments using wavelet packet transform and higher order statistics," *Progress In Electromagnetics Research*, PIER 58, 301–317, 2006.

16. Yang, F. and A. S. Mohan, "Ultra wideband microwave imaging and localization for breast cancer," *IEEE Microwave Conference, APMC 2008. Asia-Pacific 2008*, 1–4, 2008.

17. Winters, D. W., J. D. Shea, E. L. Madsen, G. R. Frank, B. D. Van Veen, and S. C. Hagness, "Estimating the breast surface using uwb microwave monostatic backscatter measurements," *IEEE Trans. on Biomedical Eng.*, Vol. 55, No. 1, 247–256, 2008.

18. Golub, G. H. and C. F. Van Loan, *Matrix Computations*, 3rd edition, Johns Hopkins, 1996.

19. GprMAX V2.0, avaliable in www.gprmax.org.

20. Hagl, D. M., D. Popovic, S. C. Hagness, J. H. Booske, and M. Okoniewski, "Sensing volume of open-ended coaxial probes for dielectric characterization of breast tissue at microwave frequencies," *IEEE Trans. Microwave Theory Tech.*, Vol. 51, No. 4, 1194–1206, 2003.